Investigation of cathode catalyst layer interfaces evolution during accelerated stress tests for polymer electrolyte fuel cells

Andrea Perego [a,b,*,1], Arezoo Avid [a,b,1], Divija N. Mamania [a,b], Yechuan Chen [a], Plamen Atanassov [a], Hakan Yildirim [c], Madeleine Odgaard [c], Iryna V. Zenyuk [a,b,*]

[a] Dept. of Chemical and Biomolecular Engineering, University of California Irvine, 221 Engineering Service Rd., Irvine, CA, 92617, United States
[b] National Fuel Cell Research Center, University of California Irvine, 221 Engineering Service Rd., Irvine, CA, 92697, United States
[c] IRD Fuel Cells LLC, 8500 Washington St. NE, Albuquerque, NM 87113, United States

ARTICLE INFO

ABSTRACT

To elucidate the evolution of ionomer-Pt and ionomer-carbon interfaces during life cycle of polymer electrolyte fuel cells (PEFCs), electrodes with high surface area (HSA) and durable carbon supports underwent catalyst and carbon corrosion accelerated stress tests (ASTs) under stoichiometric and sub-stoichiometric gas flow conditions. Electrochemical characterizations, as well as X-ray photoelectron spectroscopy (XPS) were utilized to assess degree of components degradation. Catalyst AST results revealed that Pt nanoparticles dispersed within the micro- and meso-pores and not in contact with ionomer are the main contributor to the 50% electrochemical surface area (ECSA) loss observed after 30k cycles resulting in significant polarization loss, which is much more notable in the case of sub-stoichiometric operating condition. Support AST results for HSA carbon showed severe ionomer degradation and 55% ECSA loss within the first 100 cycles, while cell with durable support exhibited negligible polarization and ECSA decay during the first 2500 cycles attributed to higher ionomer coverage, preservation of proton pathways preventing Pt from detachment.

1. Introduction

Many countries are committed to decarbonization of energy systems by 2050. Transportation sector is one of the largest emitters of carbon dioxide. Battery electric vehicles will decarbonize most of the light-duty fleet but for the heavy-duty transportation sector fuel cell electric vehicles (FCEVs) are promising. FCEVs have quick refueling time and high energy density designed for long driving range. California and other states already have existing hydrogen refueling infrastructure. Unlike passenger cars and buses that have reduced the petroleum consumption to some extent, long-haul trucks still rely heavily on diesel fuel making them responsible for a large portion of carbon dioxide emissions [1]. Polymer electrolyte fuel cells (PEFCs) stack is at the heart of the fuel cell system. For heavy-duty trucks the PEFC stack design requirements are different from existing automotive stacks: with more space available on board, power-to-weight ratio becomes subsidiary to durability aspects, since long-haul trucks must drive for up to 100,000 miles per year. Currently, the lifetime goal set by the US Department of Energy (DOE) is

8000 h for automotive stacks, 20,000 h for buses [2], and up to 30,000 h for long haul tractor-trailers [3,4]. To meet the durability criteria of 30, 000 h, further understanding of fundamental mechanisms of degradation within individual cell components is needed.

An extensive knowledge about most aspects of fuel cell durability is already present in the literature [5]. A review by Ren et al. [6] summarized most of the achievements done so far in the field and provided the current state-of-the-art research on various degradation aspects of the PEFCs. The degradation of the membrane electrode assembly (MEA) in the fuel cell stems from the interplay of various mechanisms among which are the loss of catalyst electrochemical surface area (ECSA), the corrosion of the carbon support, and the chemical and mechanical breakdown of polymeric membrane [7]. To assess the durability of a fuel cell without relying on real-time data, accelerated stress tests (ASTs) have been developed that involve voltage cycling relevant to automotive applications with intermittent performance evaluation standardized by the DOE. Because durability studies in the automotive field revolve particularly around Pt catalyst degradation and carbon-support

---

corrosion, widely-used AST protocols target the degradation of an individual component of the MEA by varying a set of operation parameters [8,9].

Many of the studies focus on catalyst or support degradation [10], but very few focus on ionomer-catalyst interface or ionomer degradation. Ionomer is used in the catalyst layers for proton conduction but its distribution in the cathode catalyst layer dictates the Pt utilization and local oxygen transport at high current densities. [11]. While the influence of ionomer physical configuration on oxygen transport to the Pt catalyst surface has been extensively explored by both experimental [12–14] and molecular dynamics simulation [15,16] tools, solid understanding of how ionomer properties change as the cell degrades is currently missing. One work from Hiesgen group focused on the degradation of ionomer using atomic force microscopy (AFM) technique showing morphological modification in the ionomer film surrounding Pt agglomerates [17]. It has been shown that the sulfonate moieties (SO_3^-) in the side chains of the ionomer can poison Pt catalyst and slow down the oxygen reduction reaction (ORR) kinetics [18]; on the other hand, the proximity of sulfonic acid groups to the catalyst surface helps transport protons that are needed for the ORR.

Various approaches have been applied to improve ionomer coverage in the cathode catalyst layer such as introducing chemically modified carbon supports with tailored porosity [19] or nitrogen containing surface [20], designing novel ionomers [21,22], and proposing various electrode fabrication processes [23,24]. In these studies, demonstration of ionomer distribution is either qualitative or is limited to modeling efforts; however, two in-situ experimental methodologies are currently present in the literature that can provide quantitative ionomer coverage data in the PEFC catalyst layers. Iden and Ohma [25] developed a method based on the double layer capacitance collected in different experimental conditions to estimate ionomer and water contributions to the proton accessibility in the cathodes. Garrick et al. [26] also used a combination of CO displacement and CO stripping procedures to evaluate the surface of the platinum that is covered with Nafion's SO_3^- groups. A work by Andersen [27] described the adsorption behavior of ionomer on platinized nano carbons and amorphous carbon using Langmuir isotherms showing that stronger adsorption of ionomer results in better durability of the catalyst but to the best of our knowledge no study explored ionomer coverage evolution during catalyst layer aging using in-situ experimental methods.

In this contribution, we utilized two analytical methods with a combination of testing protocols including catalyst AST under both stoichiometric and sub-stoichiometric gas flow conditions, and carbon corrosion ASTs to investigate the evolution of ionomer and SO_3^- groups' coverage in fuel cell cathode electrodes during cell ageing. The extensive characterization provided an insight into the changes in ionomer distribution during degradation and its influence on cell performance, ECSA loss, and ionic conductivity under harsh testing conditions. Ex-situ characterizations such as scanning electron microscopy (SEM) and X-ray photoelectron spectroscopy (XPS) were also performed at the beginning of life (BOL) and end of life (EOL) to determine the microstructure and composition of the ionomer after degradation. This work brings understanding of ionomer-catalyst and ionomer-carbon interfaces with the hope to develop durable and high-performing fuel cell electrodes for the upcoming generation of heavy-duty vehicles.

2. Materials and methods

2.1. Materials

Two types of MEA with 25 cm^2 active area were manufactured by IRD Fuel Cells LLC, specifically designed for these experiments. MEAs 1 and 2 (see Table 1) featured cathode catalyst layers with standard high surface area carbon support. MEA 1 and 2 underwent catalyst and carbon corrosion ASTs, respectively. All MEAs had ionomer to carbon (I/C) ratio of 0.8. Catalyst AST was also performed under both stoichiometric

Table 1
Parameters of the MEAs employed in this work.

	Cathode loading	Anode loading	Support type	AST type
	mg cm^{-2}	mg cm^{-2}	-	
MEA 1	0.6	0.2	HSA	Catalyst (stoichiometric condition)
MEA 2	0.6	0.2	HSA	Support
MEA 3	0.4	0.1	LSA	Support
MEA 4	0.6	0.2	HSA	Catalyst (sub-stoichiometric conditions)

and sub-stoichiometric reactant gas condition, the later one termed as MEA 4. The MEA 3 cathode catalyst was supported on durable, low surface area (LSA), graphitized carbon support, and it was employed for the support AST studies. Both MEA types have 18 µm PFSA (Gore Fuel Cell Technologies manufacturer) membrane and are loaded with Pt catalyst and PFSA-based ionomer. The details about the tested MEAs are reported in Table 1.

2.2. Fuel cell testing and characterization

Scribner 850e fuel cell test stand with maximum current load of 50 A (Scribner & Associates Inc.) was used for performing AST and measuring performance metrics such as polarization curve and mass activity. ASTs were performed according to the DOE protocols. This work focuses on two AST protocols, namely the Nissan-FCTT Pt dissolution [9] and DOE carbon corrosion cycles [28]. Pt dissolution cycle was performed at 80 °C, under fully humidified H_2/air at environment pressure [29] and 0.25/0.25 slpm gas flow-rates, with a square-wave potential profile from 0.6 to 0.95 V or OCV, whichever is smaller, with 3 s hold at each step [10]. For the starved conditions the flow rates were 0.05/0.05 slpm instead. The total number of cycles was set to 30,000 with interruptions for in-situ electrochemical characterization including polarization curves, cyclic voltammetry (CV), CO displacement/stripping, electrochemical impedance spectroscopy (EIS) for calculating double layer capacitance, and catalyst layer ionic conductivity. Characterizations were performed at the beginning of life (BOL), 1,000th, 5,000th, 15, 000th, and 30,000th cycle. Table S1 reports the summary of the testing protocols for the catalyst AST and characterization.

Carbon corrosion AST was also performed at 80 °C under fully humidified H_2/N_2, with gas flow-rates of 0.25/0.25 slpm. The potential was cycled using a triangular wave between 1 and 1.5 V with a sweep rate of 0.5 Vs^{-1}. Interruptions for the characterization were done at 100th, 500th, 1000th, 2500th, 5000th cycle under air environment [29]. In-situ electrochemical characterization included polarization curves, cyclic voltammetry (CV), CO displacement/stripping, electrochemical impedance spectroscopy (EIS) for calculating double layer capacitance, and catalyst layer ionic conductivity.

MEAs were conditioned at 80 °C and 100% RH by potential holds at 0.8, 0.6 and 0.3 V for 30 s each until the values of the current density remains constant for at least 3 consecutive cycles. Polarization curves were performed in H_2/air environment with 1.5/1.8 stoichiometric flows at 80 °C with 100% RH and 150 kPa absolute pressure. Corresponding cell voltage at each current density (0, 10, 25, 50, 100, 200, 400, 600, 800, 1000, 1200, 1400, 1600, 1800 mA cm^{-2}) was averaged over the 180 s current hold. CV was performed to assess the catalyst ECSA by sweeping the potential between 0.095 and 1 V at 20 mVs^{-1}. These measurements were performed using VSP-BioLogic 4 A potentiostat, feeding the cell with fully humidified (100% RH) H_2/N_2 gas flows (0.25 slpm flow rate on each side). Cell temperature was set to 80 °C with no backpressure applied.

2.3. Measurement of SO₃⁻ group coverage using CO

Evaluation of SO_3^- groups coverage was performed following the method developed by Garrick et al. [26]. CO displacement was preceded under fully humidified 5% H_2 in N_2 and N_2 (0.25/0.25 slpm) on the anode and cathode, respectively. 2% CO in N_2 was introduced to the equilibrated cathode electrode after 2 min hold at 0.35 V. The potential was kept for 6 more min, while recording the current. The cathode was then purged with N_2 for 20 min and subsequently, CO stripping was performed by cycling the potential between 0.095 and 1 V at 20 mV s⁻¹. The procedure was repeated in dry conditions at 25% RH. CO displacement charge was calculated from the current-time plot. When CO is introduced in the system it displaces charges on the platinum surface and a variation in the current of the cell was registered. Current-time plot was corrected by subtracting the baseline current before and after the introduction of CO to normalize the current peak to the same baseline, and finally the charge was obtained by integrating the current peak:

$$Q_{displacement} = \int_{t_0}^{t_1} i \quad dt \tag{1}$$

where t_0 and t_1 are the two timestamps chosen as the steady conditions before and after the introduction of the carbon monoxide mixture. Figs. S9, S11, S13 and S15 show the CO-displacement current densities vs. time. The value of the stripping charge obtained from the integration of the CO stripping peak, and it was used also for the calculation of the Pt electrochemical surface area with the assumption of 420 μC cm⁻² as the unit charge for integrated CO areas, as reported by [26]:

$$ECSA_{CO} = \frac{Q_{stripping}}{0.42 \times Pt \quad loading} \tag{2}$$

where $Q_{stripping}$ is the CO stripping charge. Figs. S8, S10, S12 and S14 show the stripping CVs for the MEAs in all the conditions of the testing.

The voltage at which the displacement is performed is greater than the potential of zero charge at Pt surface, which is reported to be around ~0.23 V[26]. In these conditions, the adsorbed species on the platinum that are displaced by the CO through oxidation must be negative, and therefore they are all attributed to the presence of SO_3^- groups adsorbed. The SO_3^- coverage can be calculated from the ratio of the twice of the displacement charge to the stripping charge:

$$SO_3^- \quad Coverage = \frac{2Q_{displacement}}{Q_{stripping}} \tag{3}$$

The measurement is carried out three times and only two last measurements are averaged to calculate the displacement charge and the first measurement is discarded.

2.4. Double layer capacitance and catalyst layer conductivity

Double layer capacitance (C_{dl}) was investigated for all cells following the method described by Iden et al. [25] in which the catalyst layer is simplified as a Randles circuit. The imaginary part of the impedance at low frequency region is used for obtaining the C_{dl}. This method identifies four interfaces in the fuel cell catalyst layer that contribute to the total C_{dl}, including platinum/ionomer, platinum/water, carbon/ionomer and carbon/water. Potentiostatic EIS was performed at 80 °C under fully humidified H_2/N_2 environment with gas flow-rates of 0.25/0.25 slpm on the anode/cathode, respectively. The DC potential was kept at 0.2 V with an AC amplitude of 5% of the DC potential, from a frequency of 10,000–0.1 Hz. The measurements were repeated three times for each cell in four different conditions: (i) dry condition (25%RH) before CO poisoning, (ii) dry condition (25% RH) after CO poisoning, (iii) wet condition (100% RH) before CO poisoning, (IV) wet condition (100% RH) after CO poisoning; each representing a subset of interfaces that contribute to the total double layer capacitance. Wet conditions express

the contribution of platinum and carbon contacted by both ionomer and water, while the dry conditions represent only the fraction covered by ionomer. Measurements on the CO-poisoned electrodes allow for understanding of sole carbon contribution which can be further subtracted from the total value to calculate the double layer capacitance of single interfaces:

$$C_{tot,100\%RH} = C_{C/i} + C_{C/w} + C_{Pt/i} + C_{Pt/w} \tag{4}$$

$$C_{tot,25\%RH} = C_{C/i} + C_{Pt/i} \tag{5}$$

$$C_{100\%RH, \quad poisoned} = C_{C/i} + C_{C/w} \tag{6}$$

$$C_{25\%RH, \quad poisoned} = C_{C/i} \tag{7}$$

where, subscripts C/i, C/w, Pt/i and Pt/w indicate interfaces at carbon/ionomer, carbon/water, Pt/ionomer and Pt/water, respectively. Once all the interfaces are known, the ionomer coverage on platinum and carbon can be calculated:

$$\theta_{i, \quad Pt} = \frac{C_{Pt/i}}{C_{Pt/i} + C_{Pt/w}} \tag{8}$$

$$\theta_{i, \quad c} = \frac{C_{C/i}}{C_{C/i} + C_{C/w}} \tag{9}$$

For the catalyst layer ionic conductivity calculations, EIS data was used. The impedance spectra from EIS data showed a 45° line in the high to medium frequency region where real and imaginary parts are equal, followed by a straight vertical line, representing a capacitive region. A physical impedance model, transmission line model (TLM), was used to fit the EIS data at high frequencies to measure the proton conductivity of the cathode catalyst layer [30,31].

2.5. Ex-situ characterization

SEM cross-sectional images were taken from the pristine and aged cells. Samples were prepared by peeling off GDLs from the MEAs, and subsequently embedding small pieces into epoxy resin (Araldite 502 epoxy resin, SPI Chem.). Samples were cut with slow speed SiC circular saw (South Bay Technologies inc.) and the sections were polished with P800, P1500, P3000 grit sandpaper, and later with 30 μm and 0.5 μm alumina paste. Cross sections were contacted to SEM stubs using silver conductive in, and SEM images were collected using Hitachi Ultra-High-Resolution SEM Regulus 8230.

The XPS data were measured by Kratos AXIS Supra X-ray photoelectron spectrometer, with a monochromatic Al Kα operating at 225 W for survey spectra and 300 W for high-resolution spectra. The survey spectra were acquired using 160 eV pass energy, 1 eV step size, 100 ms dwell time, while the high-resolution spectra were acquired using 20 eV pass energy, 0.1 eV step size, and 100 ms dwell time. For each spectrum, the data were averaged by three random sample points and each sample point was averaged by specific cycles of scanning. All spectra were analyzed using CasaXPS software and fitted with 70% Gaussian / 30% Lorentzian line shape.

3. Results and discussion

3.1. Catalyst AST

Catalyst AST was performed on MEA 1, where the cell was cycled 30,000 times. Pt underwent oxidation, dissolution and ripening. ECSA and ionomer coverage were recorded at defined intermediate steps. The Nissan-FCTT Pt dissolution cycle is designed to trigger the dissolution and re-deposition of the catalyst. Fig. 1 shows the polarization performance and high frequency resistance (HFR) of the cell at the BOL during the catalyst AST protocol. Most of the polarization loss occurred during the first 5,000 cycles in the kinetic and Ohmic regions. This is consistent
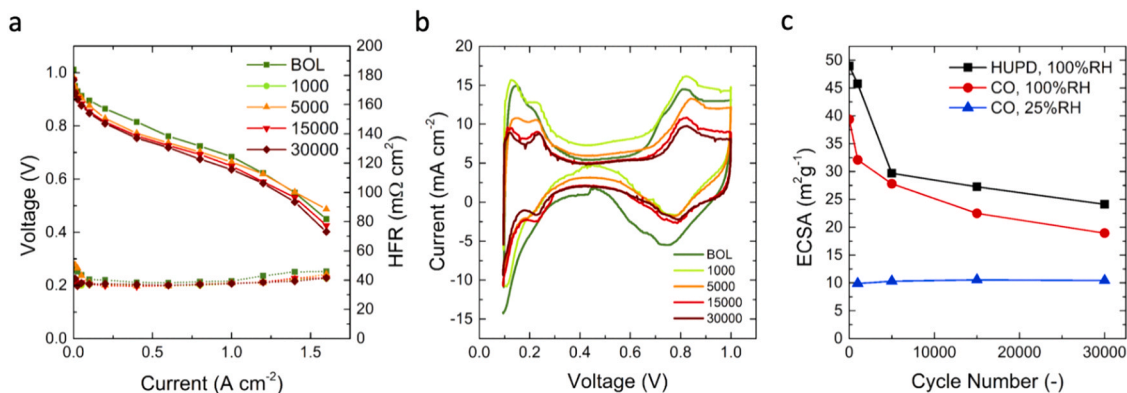
Fig. 1. Electrochemical properties of MEA 1 collected at different stages of the catalyst AST: a) polarization curves at 80 °C, 100 RH, 1.5/1.8 stoichiometric flows with 150 kPa absolute back-pressure, b) cyclic voltammograms, c) evolution of the ECSA determined by both H_{UPD} region of the H_2/N_2 CV and CO-stripping charge at indicated RH.

with the changes in the ECSA, shown in Fig. 1c, where a sharp decrease is observed for the first 5,000 cycles and then more gradual ECSA loss is observed with both CO-stripping and H_{UPD} methods under wet conditions. Therefore, the polarization loss observed in kinetic and Ohmic regions is largely due to ECSA loss. The cell voltage loss from the BOL to 30,000 cycles throughout entire polarization curve was less than 0.1 V, for example, at 0.2 A cm^{-2} the voltage loss was about 70 mV. Overall, after 30,000 cycles, MEA 1 lost 50% of its ECSA, as measured in wet conditions, it was reduced from 50 to 25 m^2 g^{-1} as measured by CV and 40–20 m^2 g^{-1} as measured by CO-displacement. However, in dry conditions the ECSA did not change and remained at around 10 m^2 g^{-1}. Under dry conditions, one detects Pt in contact with ionomer but not with water. Pt that is in micro- and meso-pores is mainly in contact with water and under dry conditions there is no condensed water to conduct ions.

The cell voltage from Fig. 1a at higher current densities than 1.5 A cm^{-2} increased at 5,000 cycles and then decreased after 15,000 and 30,000 cycles. This is possibly due to improved wettability of the catalyst layer as shown by slightly reduced HFR at high current densities for 5,000 cycles and after, due to better proton accessibility to the catalyst or better oxygen transport. From the shape of the H_{UPD} region displayed in Fig. 1b, it can be shown that the first H_{UPD} peak decreased more with the number of cycles. This is generally associated with the changes in the 110 and 111 Pt facets, where the surface of the Pt is rearranging by the loss of high energy facets and the increasing amount of lower energy facets [32] caused by the dissolution/redeposition of Pt during AST protocol.

Fig. 1c exhibits the difference in ECSA obtained from dry and wet measurements, which is most likely due to the difference in the amount of Pt within the micro- and meso-pores and that on the surface of the high surface area carbon. As already mentioned, for 25% RH most of the detected ECSA is attributed to Pt on the surface of the carbon and not within the carbon support pores. The ionomer polymer chains are in the range of tens of nanometers in diameter and cannot penetrate the meso and micropores of the carbon support due to the size exclusion [12] and only water is expected to conduct ions in the micro- and meso-pores. For 25% RH, we expect no liquid water condensation in the pores and hence Pt in the pores will not be detected by the ECSA measurements. By comparing the ECSA value at the BOL in dry and wet conditions, which is about 10 and 40 m^2 g^{-1}, respectively (determined by dry and wet CO measurements), one can conclude that most of the nanoparticles (about 75% of them) are dispersed inside the micro- and meso-pores of the carbon support and are not accessed by the ionomer. Furthermore, while the total surface area under 100% RH decreases with cycling, the area contacted by the ionomer (determined by dry CO measurements) remains constant. Several conclusions can be derived from this data: (i) Pt in contact with ionomer does not degrade or/and (ii) Pt dissolves from

micro- and meso-pores and redeposits in the areas with ionomer coverage but Pt still dissolves from under ionomer. It is possible that positively charged Pt ions are expelled from the micro- and meso-pores with positive pore surface charge at these high potentials and then redeposited in the locations where sulfonic acid groups partially balance surface positive charge.

Fig. 2a shows the variation of the double layer capacitance for MEA 1 under wet and dry conditions. Double layer capacitance for wet condition includes all interface, such as Pt/i, Pt/w, C/i and C/w. The double layer capacity for 100% RH was 300 mF cm^{-2} at the BOL and it decreased to 175 mF cm^{-2} after 30,000 AST cycles. ECSA loss amounted to 50% from the BOL to 30,000 cycles, and double layer capacitance loss was about 40%, indicating that C/i and C/w double layer capacitance cannot be neglected. The double layer capacitance for dry conditions was 75 mF cm^{-2} and it was reduced to 30 mF cm^{-2} after 30,000 cycles. The ratio of double layer capacitance in wet and dry conditions is similar to that of wet and dry ECSA which is about 4. The double layer capacitance data is in alignment with the ECSA data confirming that about 75% of the Pt particles are in contact with water and the remaining 25% of Pt particles are in contact with the ionomer.

Fig. 2b shows the evolution of the ionomer coverage on Pt and carbon obtained from the difference between the double layer capacitances at various RH, as described in Section 2. About 50% of accessible carbon area is covered by ionomer, indicating that the remaining 50% is covered by water. This agrees with the carbon support having high surface area. The fraction of C/i interface remained constant from the BOL to EOL, as catalyst AST does not have a strong effect on carbon corrosion. The Pt/i interface fraction decreases with the AST cycling. At the BOL, the Pt/i interface is about 20%, whereas the remaining 80% is Pt/w interface. The ionomer coverage here agrees well with the ECSA and double layer capacitances data. At 15000 AST cycles, the ionomer coverage increased to 38% but decreased to below 10% at 30,000 cycles because the ionomer coverage is a relative value and the sum of Pt/i and Pt/w must be equal to 100%. At 15000 cycles, the relative fraction of Pt/i increased as Pt has been lost from the micro- and meso-pores (indicated by wet ECSA), where it was in contact with water. The loss of Pt/i at 30,000 cycles can potentially be due to ionomer degradation, which will be explored when the XPS data is discussed.

The evolution of SO_3^- coverage on Pt is reported in Fig. 2c. This coverage is different from the ionomer coverage, as it shows only the fraction of the Pt surface that the side chain of the PFSA-based polymer is adsorbed on, as described by Eq. (2). While ionomer presence is generally favorable for a better local proton transport, adsorption of SO_3^- groups is reported to suppress ORR reaction [33]. The two parameters appear to be related to each other: one may assume the adsorption of sulfonic groups is a direct consequence of the ionomer coverage on the platinum catalyst [22], but too much of it may lead to an
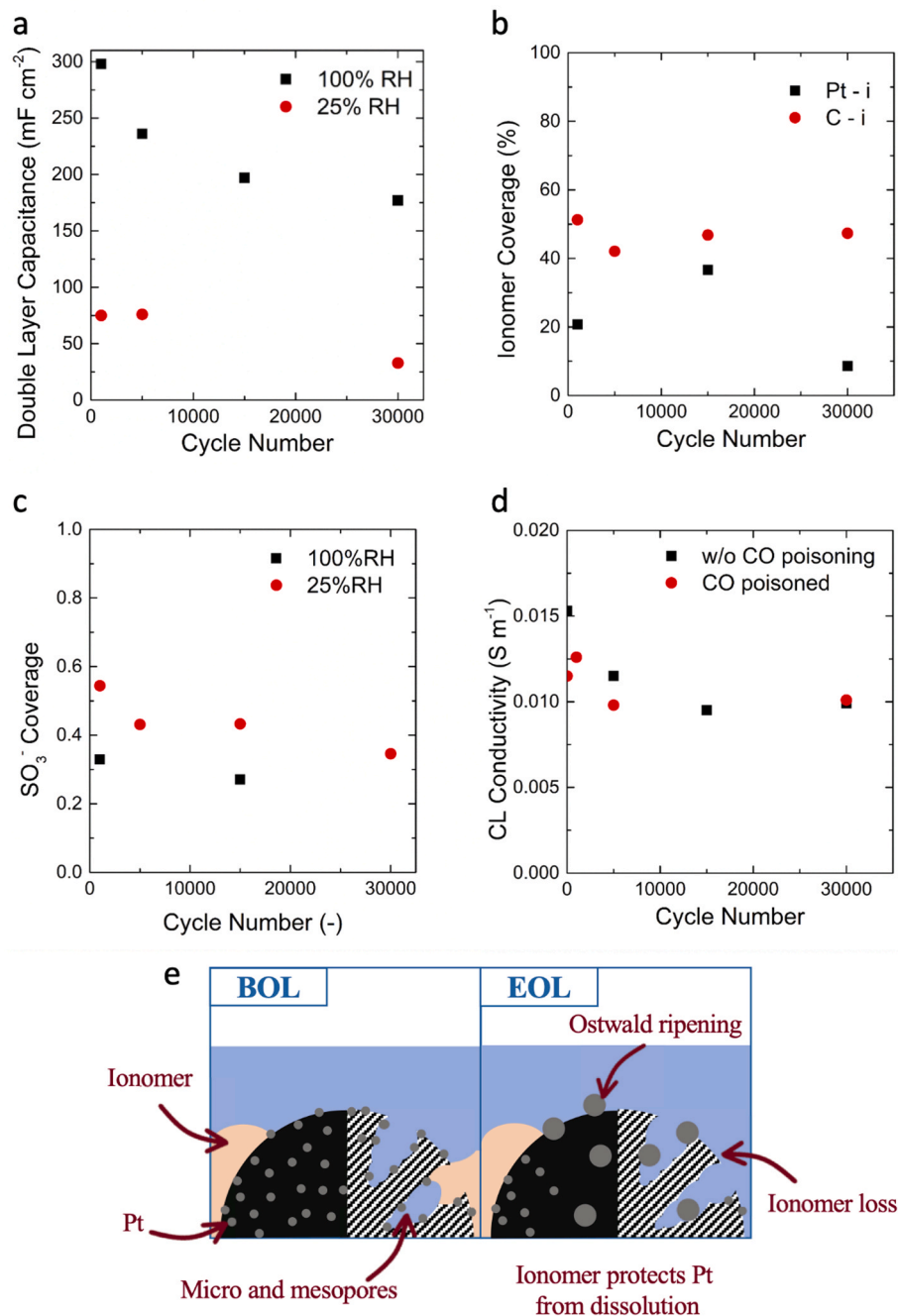
Fig. 2. a) Double layer capacitance for MEA 1 for humidified and dry conditions, b) ionomer coverage for MEA 1 on platinum and carbon support, c) SO3- coverage on Pt surface for the specified RH values, d) catalyst layer conductivity at 25% RH from the EIS for MEA 1 with and without CO. e) A schematic of the proposed degradation phenomena occurring for MEA 1 subjected to catalyst AST.

excessive poisoning of the active sites, so there is likely to be an optimal value that ensure the best proton accessibility, with limited effect on catalytic performance. Both in the wet and dry cases, the SO_3^- coverage on Pt is decreasing with AST cycles. For 100% RH at the BOL, the SO_3^- coverage on Pt is 0.32, which is similar to what has been reported in literature [26,34]. At 15000 cycles, the SO_3^- coverage decreased to 0.25 in wet conditions. As can be seen, some SO_3^- coverage data points are not available due to the complexity of the measurements and the fact that reproducibility was not achieved for these points. Similar decreasing trend in SO_3^- coverage on Pt was observed for 25% RH, but the ionomer coverage was much higher. This is because of low CO-stripping charge on Pt at 25% RH. As can be seen from Eq. (2), the SO_3^- coverage is proportional to the ratio of CO-displacement and CO-stripping. For both

100% and 25% RH, the CO-displacement charge is similar (Fig. S2 and Table S2 in Supplementary Material (SM)), but CO-stripping charge is much higher for 100% RH as Pt that is covered by water in the micro- and meso-pores is detected in wet conditions. We also observe the CO-stripping charge (proportional to ECSA values from Fig. 1) does not change with AST cycling at dry conditions. The SO_3^- coverage on Pt at 25% RH decreased from 0.55 to 0.35. This decrease is due to reduction in CO-displacement charge (absolute value). This decrease in the coverage can be attributed to a chemical degradation of the ionomer itself. It is reported in the literature that at high potentials, OH radicals react with Nafion side chains and contribute to degradation of the membrane [35]; therefore, ionomer is also affected. This is supported by XPS analysis in Fig. 3a by comparing the changes in the intensity of C-F
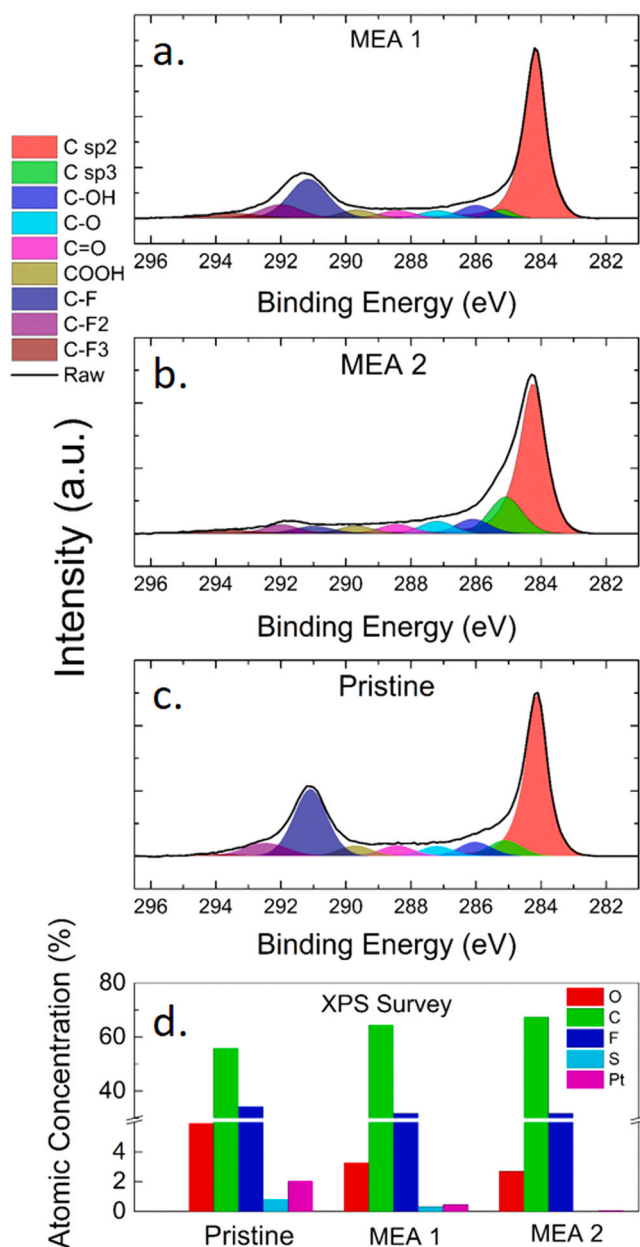
Fig. 3. a) XPS of carbon for MEA 1, b) MEA 2 and c) pristine MEA. d) Elemental survey for the three MEAs.

bond peak with the pristine case in Fig. 3c, where we see a decrease in intensity. This peak is related to the bond between C and only one fluorine, which corresponds to the position in the PTFE backbone where the side chain is present. From the elemental survey in Fig. 3d, we also register a smaller atomic concentration of sulfur, which indicates the loss of side chains and SO_3^- groups.

Fig. 2d shows the evolution of the ionic conductivity in the catalyst layer obtained from the EIS spectra fitting for dry conditions. This ionic conductivity captures only ionomer and not water clusters that can connect the disconnected ionomer segments. The ionic conductivity of the catalyst layer does not change significantly during AST cycling and was around 0.01 – 0.015 S m^{-1}. EIS data was available for catalyst layer as is, and also after CO-poisoning. Both show similar trends with the loss of ionic conductivity within first 5000 cycles and then leveling off conductivity values from 5000 to 30,000 cycles.

In summary, behavior of ionomer in the cathode catalyst layer during a catalyst AST can be summarized by Fig. 2e. Pt dissolution reaction

is triggered by the voltage cycling but the dissolution rates are different for Pt in contact with ionomer vs. Pt in contact with water (in micro- and meso-pores). Higher dissolution rates are observed for Pt in contact with water, perhaps due to higher Pt ions transport in confined water environment in micro- and meso-pores that can be affected by electric double layers and surface charge (positive for high applied potentials). In parallel, due to the high potential and production of OH radicals, some ionomer loss is observed because of the chemical attack, resulting in loss of SO_3^- group coverage on the platinum surface. Transmission electron microscopy (TEM) using Jeol Grand Arm has been performed on the pristine and aged MEA 1. The results are shown in Fig. S1, where particle size distributions were reported, as an average over multiple images collected over various locations. From the particle size analysis, the mean particle size increased from 3 nm for pristine MEA to around 6 nm for aged MEA. For aged MEA 1 one observes a broad particle size distribution range, ranging from 2 nm to 14 nm. This might be due to protective effect of the ionomer over the small platinum particles. From the TEM image it is not possible to discern which particles are covered or not covered by ionomer. The inhomogeneity in particle size partially supports the conclusion on different modes of degradation for Pt covered and not covered by ionomer.

Fig. S3 in SM displays the polarization curves, CVs, Tafel plots and ECSA loss for MEA 4, which was subjected to starvation conditions in terms of gas flow. MEA 4 was identical to MEA 1 but used 5 times lower gas flow-rates during catalyst AST. The polarization loss and ECSA loss was observed to be more dramatic for MEA 4 compared to MEA 1. Voltage loss in some polarization regions between BOL and EOL was higher than 100 mV. At 0.2 A cm^{-2} cell voltage difference between the BOL and EOL was close to 100 mV, compared to only 70 mV for MEA 1. The ECSA loss was 60–63% at wet conditions and for dry conditions it was about 50%. Similar to MEA 1 majority of ECSA loss happened within 5000 AST cycles. Unlike MEA 1, this reactant starved MEA has seen increase in HFR at 15000 and 30,000 cycles. Fig. S4 shows the changes in double layer capacitances, ionomer coverage, sulfonic acid group coverages and catalyst layer conductivities for MEA 4. For most of these similar trends are observed with the MEA 1 but for SO_3^- coverage that did not show trend. Fig. S5 shows the decrease in C-F bond intensity from BOL to EOL, indicating that MEA 4 similarly to MEA 1 had ionomer degradation. High gas flow-rates are important during the AST as they ensure the stable potential of the anode and uniform along-the-channel conditions for both anode and cathode. Otherwise, the AST will be conducted in inhomogeneous conditions for gas flow along the channel and heterogeneous degradation of catalyst layers will occur.

3.2. Carbon corrosion AST

During carbon corrosion AST, the cell voltage is swept between 1 and 1.5 V. In this condition, Pt is almost fully oxidized on the surface and does not participate in the degradation phenomena; thus, we can expect that most of the ECSA loss be attributed to the corrosion of the support that disconnects the catalyst from the electron and proton pathways. Fig. 4a shows the polarization performance of the MEA 2 during the first 1000 carbon corrosion AST cycles. Dramatic loss of the polarization is seen between 100 and 500 cycles; however, no increase in the HFR was observed. The HFR increased significantly between 500 and 1000 cycles because of the lack of electron and proton pathways after carbon corrosion. This does not seem to induce a major limitation to the cell performance because most of the losses are observed prior to the HFR increase. ECSA, as can be seen from the CV plots in Figs. 4b and 4d, had a steady decrease up to 500 cycles, where the cell lost half of its initial active Pt surface, and then stabilized for the remaining 500 cycles. MEA 1 and 2 show similar ECSA in wet condition, while the dry ECSA is slightly higher for MEA 2 compared to MEA 1. The ECSA loss is also observed at 25% RH, indicating that Pt/i interface is also reduced during support AST. The CVs are similar for MEA 1 and MEA 2, as predominantly the first H_{UPD} peak (Pt(110)) is lost during the AST. However, a
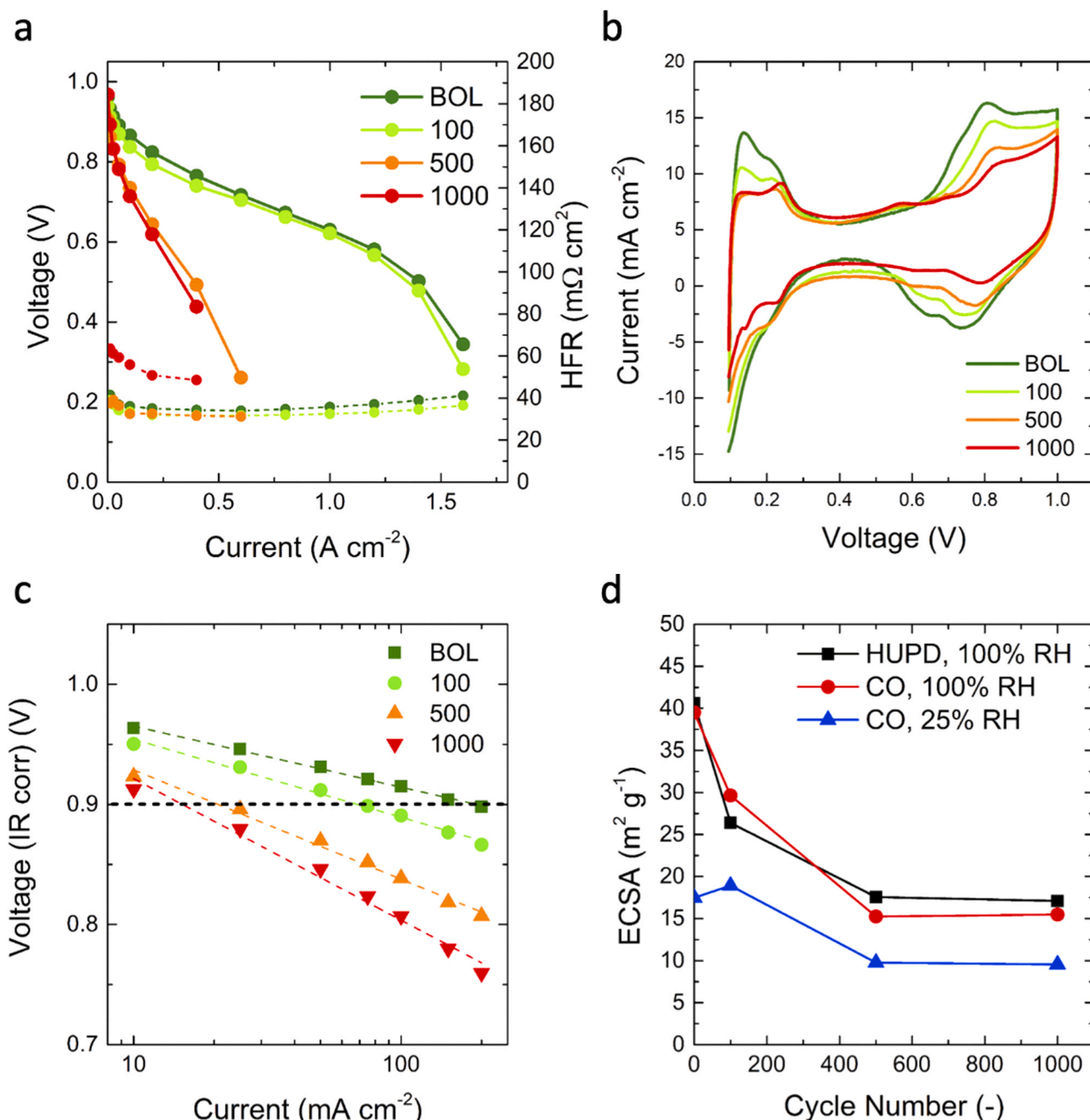
Fig. 4. Electrochemical properties of MEA 3 collected at different stages of carbon corrosion AST: a) polarization curves, b) cyclic voltammograms. c) oxygen polarization curves. d) ECSA evolution for MEA 2 collected from HUPD and CO stripping for the indicated RH values.

distinct feature on the CV is observed for MEA 2 at 500 and 1000 cycles, at around 0.6 V that is attributed typically to carbon oxidation.

Similar dramatic loss in polarization is observed in H_2/O_2 as shown by Fig. 4c, where the IR-corrected I-V curves are reported on the x-log scale. The slope of the curves is the Tafel slope that represents the mechanism of ORR (number of electrons that participate in reaction), assuming a single rate-determining step and that all the losses are kinetic in nature. The Tafel slopes are tabulated in Table 1, where Tafel slopes change from 50.8 mV dec^{-1} at the BOL to 133 mV dec^{-1} at 1000 cycles. Since, the catalyst composition did not change, there is no reason for the reaction mechanism to change. The only explanation for the increased Tafel slope is that at higher cycles (500 and 1000), transport and ohmic limitations become significant. The mass and specific activities (per geometric area) also show dramatic decrease between 100 and 500

cycles. A sharp decrease in the catalytic activity seems to be the main factor that determines the degradation of the cell. This should be attributed to the Pt ECSA loss (about 50%) due to the failure of the support during corrosion, disconnecting and mechanically removing Pt particles. From the ECSA plot, an ECSA loss of 10 m^2 g^{-1} is observed from the BOL to 1000 cycles, but the polarization behavior does not change significantly with a small decrease in kinetic region. However, when ECSA was further reduced to 15–17.5 m^2 g^{-1} in wet conditions at 500 and 1000 cycles, this is where the catastrophic polarization loss was observed. The large kinetic loss is apparent in both Fig. 4a and Fig. 4c. When using Tafel model for the ORR kinetics, one can derive equation where the loss in overpotential per decade of catalyst loading corresponds to the value of Tafel slope. [36] The ECSA ratio at the BOL to that at 500 cycles is about 3; therefore, the effective loss of loading is most

likely similar to this ratio. From Table 1, about 22 mV (Tafel slope of 65 mV dec^{-1} divided by 3) is expected to be lost as overpotential due to the reduction in the ECSA between the BOL and 500 cycles and the actual loss at 10 mA cm^{-2} (from Fig. 4c) is close to this value and is 38 mV. The loss of ECSA explains the increase in overpotential in the kinetic regime, but it does not explain the increase in the Tafel slope (Table 1 and Fig. 4c) and progressively higher overpotential losses in the Ohmic region that cannot be elucidated by the HFR as the HFR value is very similar at the BOL and after 500 cycles.

Fig. 5a shows the double layer capacitance trend as a function of AST cycles and the decrease of the double layer capacitance for wet conditions is similar to that of MEA 1. At the BOL, the double layer

capacitance was 300 mF cm^{-2} (also 300 mF cm^{-2} for MEA 1) and it decreased to about 175 mF cm^{-2} at 1000 AST cycles. At 25% RH, MEA 2 showed higher double layer capacitance of 130 mF cm^{-2} at the BOL while MEA 1 exhibited a double layer capacitance of 75 mF cm^{-2}. This indicates that MEA 2 has more Pt on the surface compared to the Pt in contact with ionomer, which is most likely due to MEA to MEA variability. Dry conditions show an initial slight increase in the double layer capacitance from BOL to 100 cycles followed by a decrease. This might be attributed to a higher Pt area becoming exposed to the ionomer at 100 cycles due to carbon corrosion, followed by Pt and ionomer loss as the support degrades after 100 AST cycles.

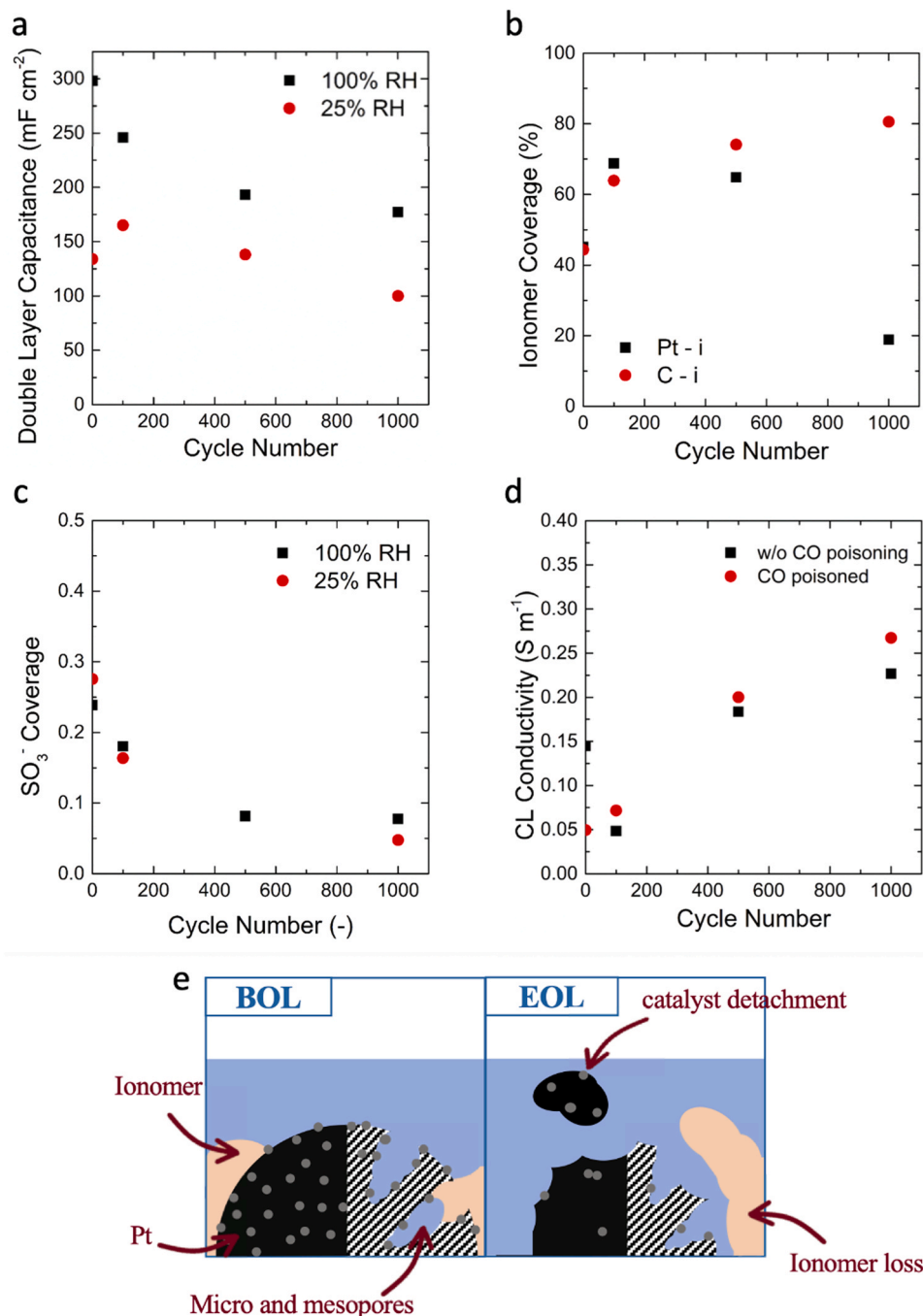Fig. 5b shows ionomer coverage as a function of number of cycles. At

Fig. 5. a) Double layer capacitance for MEA 2 for humidified and dry conditions, b) ionomer coverage for MEA 2 on platinum and carbon support, c) SO$_3^-$ coverage on Pt surface for the specified RH values, d) catalyst layer conductivity at 25% RH from EIS for MEA 2 with and without CO poisoning. e) A schematic of the proposed mechanism of degradation for the carbon support AST.

the BOL, the C/i for MEA 2 is 45%, which is close to the C/i value of 50%. for MEA 1. However, as already mentioned, Pt/i double layer capacitance is higher for MEA 2 compared to MEA 1 at the BOL. The C/i percentage increases with the cycle number. This increasing trend is due to the reduction in "free" carbon surface after corrosion, increasing the fraction of the total that is contacted by the PFSA polymer. After 1000 cycles, 80% of carbon surface is covered by ionomer and only 20% is covered by water. Ionomer coverage on Pt first increases from 45% to 69% from BOL to 100 cycles, and then decreases to 20% at 1000 cycles. The Pt/i trend is similar to the dry ECSA and double layer capacitance trends: in the initial cycles more Pt surface is exposed to the ionomer before the drastic degradation of the polymer and support that causes disconnection of both proton and electron pathways.

SO_3^- coverage in wet conditions is similar for MEA 1 and MEA 2 at the BOL. Since more Pt is present on the surface of carbon in MEA 2, the

SO_3^- coverage in dry and wet conditions is very similar. The coverage shows a severe decrease of around 90% over the 1000 cycles. The same trend of decrease in the ECSA was also observed for wet conditions. The CO-stripping charge mostly shows the decreasing trend with increase in the cycle number due to loss of Pt surface area (Fig. S2b). The absolute value of the CO-displacement charge is very similar for wet and dry conditions and monotonically decreased for MEA 2. Since both CO-displacement and stripping charges decreased with AST cycling number, the net SO_3^- coverage decrease is large, indicating the loss of Pt/i interface due to both Pt and ionomer loss (Fig. S2b). From the XPS data in Fig. 3b, the intensity of C-F bond peak is significantly reduced for MEA 2 compared to Baseline, indicating the loss of the side chains in the ionomer. The fluorine content is reduced but sulfur atomic relative percentage is extremely low, showing additional proof of ionomer degradation. Ionomer loss for MEA 2 is larger than that of MEA 1 (Pt
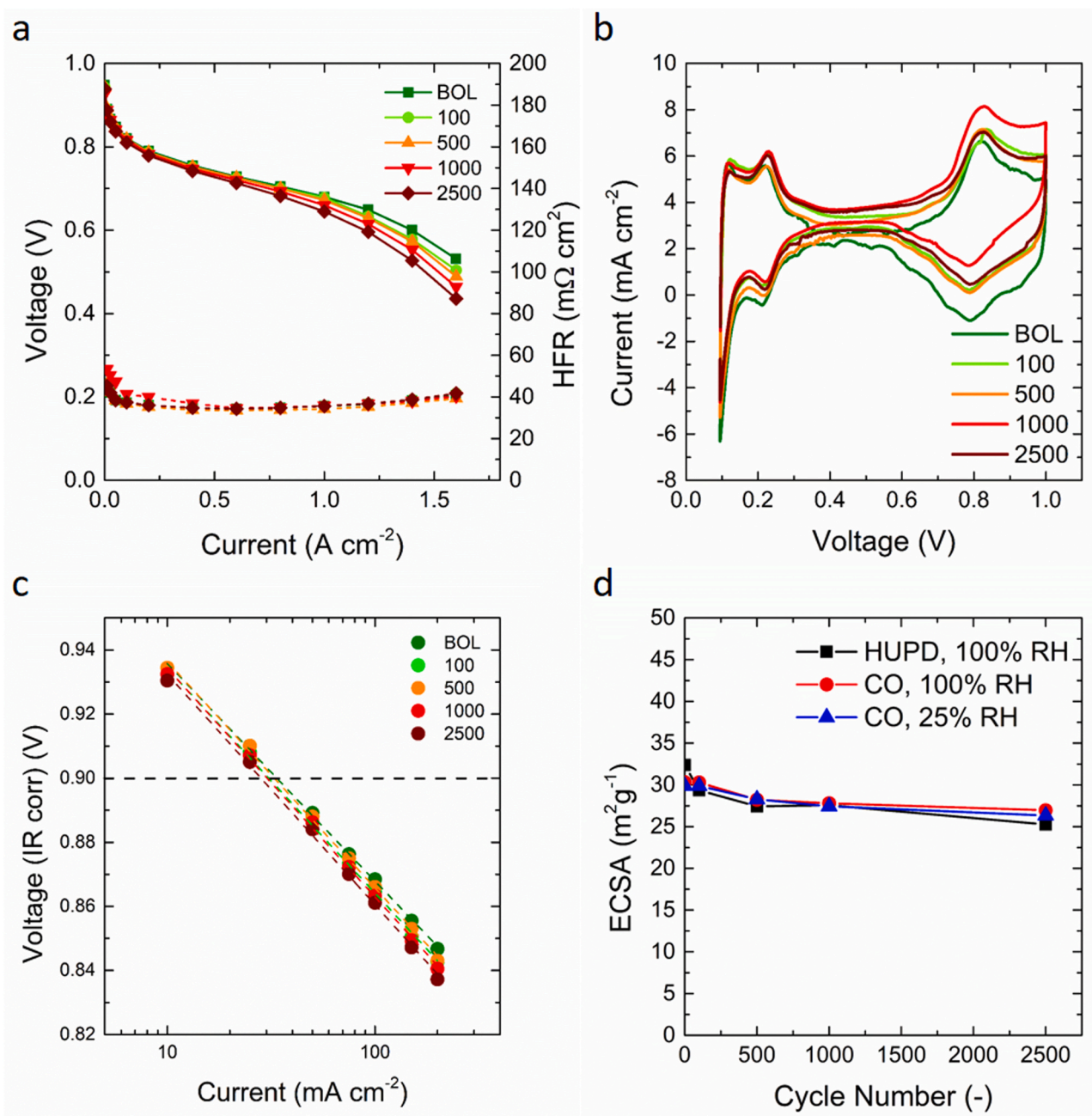

Fig. 6. Electrochemical properties of MEA 4 collected at different stages of carbon corrosion AST: a) polarization curves, b) cyclic voltammograms c) mass activity plots from oxygen polarization curves, d) evolution of the ECSA determined by both HUPD region of the H_2/N_2 CV and CO stripping charge at indicated RH.

dissolution AST case). We can attribute this to higher potential of the carbon corrosion AST and therefore an enhanced production of radicals which offers much harsher conditions to the polymer. One might argue if this could be factored in to attribute the source of degradation that comes from this type of accelerated stress tests: the effect of ionomer loss and the disconnection of pathways for protons might be of the same order of magnitude compared to the loss of active material and ECSA. This is reflected directly in the loss of polarization as shown in Fig. 4c.

Catalyst layer conductivity from Fig. 5d shows a monotonic increasing trend that can be explained by the thinning of the catalyst layer due to carbon corrosion, leaving shorter ionic pathways that results in a better ionic conductivity. The thickness reduction in the catalyst layer after carbon corrosion experiment is shown by Fig. S7, SM. As summarized in Fig. 5e, during support AST, the high potential on the cathode leads to the corrosion of the carbon in the electrode, resulting in the detachment of catalyst particles with the loss of active sites. At the same time, both for mechanical degradation and chemical attack, the ionomer is also deteriorating, progressively eliminating access for protons to the remaining active Pt sites. The two combined effects lead to a severe loss in polarization performance, as well as a sharp ECSA loss in the first one hundred cycles.

Carbon corrosion AST on MEA 3 was performed to show the behavior of a corrosion-tolerant cathode having LSA carbon support compared to the HSA carbon support of MEA 2. Fig. 6a displays the polarization performance during the first 2500 AST cycles. The cycling was interrupted between 2500 and 5000 cycles due to a shunt that short circuited the cell, unrelated to the degradation phenomena. In this set of polarization curves, it is possible to see how both the activation and ohmic regions are not changing significantly and therefore we can assume both kinetic properties and electric conductivity are preserved in the cell. From H_{UPD} region in Fig. 6b, no dramatic change in the Pt features was observed, and from mass activity plots in Fig. 6c, the current values at 0.9 V show little change overall, indicating only minor decrease in the kinetic performance of the catalyst. The measured Tafel slopes did not change significantly with cycling, increasing from 67.9 mV dec^{-1} at the BOL to 71.9 mV dec^{-1} at 2500 cycles. Degradation is mostly limited to the high current density region, where the cell shows mass transport limitations. This might be due to carbon oxidation and flooding. The ECSA measured with H_{UPD} and CO-stripping is plotted as a function of AST cycle number. BOL ECSA was measured to be around 30 m^2 g^{-1} for both 100% and 25% RH. The stability comes at the cost of a lower initial ECSA: graphitized carbon generally is less porous compared to other types of support [37] and it is more difficult to disperse Pt uniformly on it. For this graphitized cathode carbon support, most of the Pt was on the surface of carbon because graphitized support had minimum amount of meso- and micro-pores [37]. After 2500 carbon corrosion AST cycles, the ECSA decreased to 27.5 m^2 g^{-1}, which is a negligible loss of surface area, showing that the graphitized support is very durable. Table 2 also revealed that mass activity and specific activities show virtually no change with number of cycles, again indicating that the graphitized support is very well designed to protect Pt from dissolution. Table 3.

Fig. 7a shows the double layer capacitance for MEA 3 in both 100% and 25% RH. Although, most of Pt is on the surface of carbon, not all of it is in contact with ionomer as there is about two times higher double layer capacitance at 100% RH compared to 25% RH. The BOL double

layer capacitance in 100% RH was 95 mF cm^{-2}, which is three times less than for MEAs 1 and 2. The graphitized support has lower double layer capacitance due to non-porous nature of the carbon support, lower Pt surface area reducing Pt's contribution to the double layer capacitance. The double layer capacitance for 100% RH first increased to 120 mF cm^{-2} at 1000 cycles and then reduced to 85 mF cm^{-2} at 2500 cycles. The increase in double layer capacitance during the first 1000 cycles was most likely due to oxidation and wetting of carbon. The double layer capacitance for 25% RH stayed at about 50 mF cm^{-2} for the entire AST, indicating very stable C/i and Pt/i interfaces. The ionomer coverage on carbon was as high as 80% or higher, which was much higher than that of MEA 1 or 2, as there were no pores within graphitized carbon and most of the carbon surface was in contact with ionomer. The Pt/i coverage was also higher for MEA 3 compared to MEAs 1 and 2, as most of the Pt was on the surface of carbon and was accessed by the ionomer. At the BOL, 50% of Pt was in contact with ionomer and after 2500 cycles, it increased to 58%. SO$_3^-$ coverage on the other hand (Fig. 7c), was only about 10% at the BOL, which is much lower compared to MEAs 1 and 2. High value of Pt/i double layer capacitance and low SO$_3^-$ coverage was most likely due to the different ionomer orientation near the surface of Pt. Carbon wettability also controls ionomer orientation near the surface [19,20].

CO-displacement charge was very similar for 25% and 100% RH. CO-stripping charge was also similar for 25% and 100% RH (Fig. S2d and Table S2). Nevertheless, although the ECSA remained constant after 2500 cycles, CO-displacement charge reduced at both RH conditions. For this MEA, the ionomer was most likely to degrade due to radicals' formation and chemical attack alone, rather than the combined effects of the loss of carbon support or Pt ECSA. Fig. S6 represents the XPS spectra for this MEA compared to the Baseline, which was identical for MEA 1 and 2. Higher content of carbon and lower content of oxygen as well as the signature of graphitized carbon support can clearly be seen in MEA 3 XPS spectra. Lower sulfur (S) signal can be indicative of ionomer degradation. This MEA also exhibited higher catalyst layer ionic conductivity at the BOL (Fig. 7d) compared to MEAs 1 and 2, which is due to the better ionomer coverage on the low surface area of carbon, as shown earlier by Ramaswamy et al. [38]. Ionic conductivity did not change significantly with cycling, when no CO was introduced into the system. To summarize, as opposed to high surface area carbon, this class of graphitized support catalysts (Fig. 7e), not only had a better tolerance to corrosion, which prevented Pt from detachment, but at the same time helped keep the polymer adhesion, maintain the ionomer content in the electrode, preserve ionic pathways and ionic conductivity, and prevent further polarization loss.

4. Conclusions

This work aimed to understand the evolution of Pt-ionomer and carbon-ionomer interfaces undergoing catalyst AST and carbon corrosion AST. Two MEAs with HSA carbon support on the cathode were subjected to the ASTs of DOE platinum dissolution protocol in air environment one of which was under gas starving condition. Two MEAs, one with HSA and one with durable graphitized carbon support (LSA support), underwent carbon corrosion AST. Electrochemical characterization at different stages of the ASTs was performed and ionomer and

Table 3
Slope and $i_{0.9\,V}$ from IR corrected I-V curves in H$_2$/O$_2$ for MEA 3.

Cycles	Tafel Slope, absolute value (mV dec^{-1})	$i_{0.9\,V}$ (mA cm$^{-2}_{geo}$)	Mass Activity (mA mg^{-1})	Specific Activity (mA cm$^{-2}_{Pt}$)
0	67.9	33.79	112.6	0.278
100	70.1	30.88	102.9	0.255
500	70.6	32.88	109.6	0.291
1000	71.3	30.24	100.8	0.270
2500	71.9	28.31	94.37	0.263

Table 2
Slope and $i_{0.9\,V}$ from IR corrected I-V curves in H$_2$/O$_2$ for MEA 2.

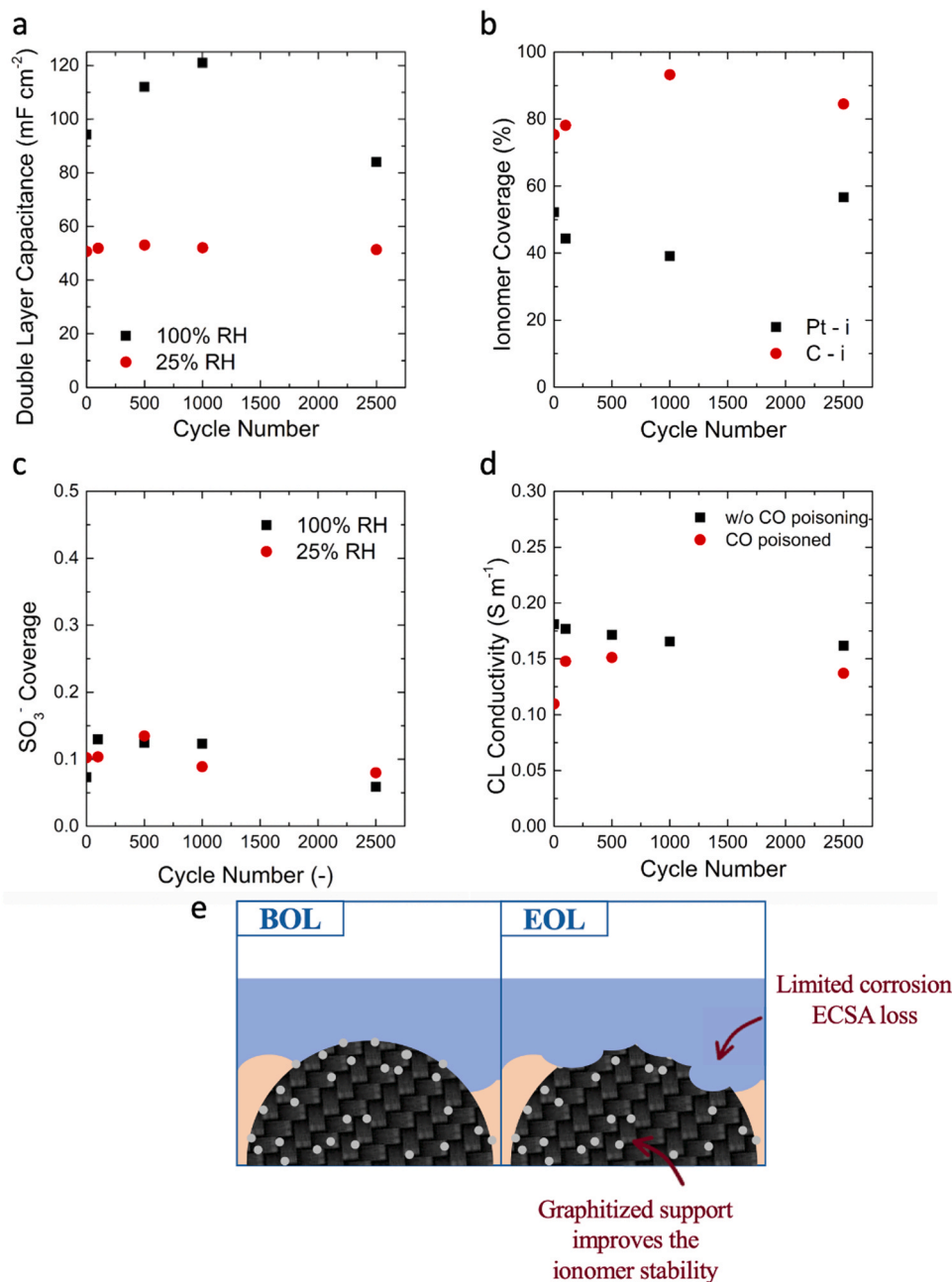| Cycles	Tafel slope, absolute value (mV dec^{-1})	$i_{0.9\,V}$ (mA cm$^{-2}_{geo}$)	Mass Activity (mA mg^{-1})	Specific Activity (mA cm$^{-2}_{Pt}$)
0	50.8	192.1	320.1	0.486
100	65.0	67.73	112.9	0.229
500	91.1	20.76	34.6	0.137
1000	133	15.96	26.6	0.104

Fig. 7. a) Double layer capacitance for MEA 3 for humidified and dry conditions, b) ionomer coverage for MEA 3 on platinum and carbon support, c) SO_3^- coverage on Pt surface for the specified RH values, d) catalyst layer conductivity at 25% RH from EIS for MEA 3 with and without CO poisoning. e) A schematic of the proposed mechanism of degradation for the carbon support AST.

SO_3^- coverage on Pt were investigated. Double layer capacitance, ionomer and SO_3^- coverages were measured in wet (100% RH) and dry (25% RH) conditions. And furthermore, Pt/i and C/i interfaces were elucidated by use of CO poison during EIS measurements. In wet conditions all Pt and carbon is contacted by either ionomer or condensed water. In dry conditions Pt and C that is not contacted by ionomer will not be detected. This study was the first one to understand Pt/i, C/i, Pt/w and C/w interfaces evolution during ASTs.

Pt dissolution AST performed on a HSA carbon support cathode (MEA 1) revealed a limited polarization loss throughout polarization curve (<70 mV), most likely attributed to the ECSA decrease under wet conditions, which was around 50% from the BOL to the EOL, defined by 30,000 AST cycles. For this MEA with HSA carbon support the following observations were obtained:

- Most of the Pt nanoparticles were in the micro- and meso-pores, as detailed by differences in ECSA (40 vs. 10 $m^2\ g^{-1}$ for wet vs. dry) and double layer capacitances (300 vs. 75 $mF\ cm^{-2}$) in wet and dry conditions.
- Pt that was not in contact with ionomer (in micro- and meso- pores) degraded more compared to Pt in contact with ionomer, as evidenced by ECSA loss, double layer capacitances and ionomer coverage for wet and dry conditions.
- For dry conditions no Pt ECSA loss was observed during AST, indicating that Pt in contact with ionomer did not degrade significantly
- Ionomer degradation was observed especially for 30,000 cycles, resulting in both Pt/i interface loss and also loss in SO_3^- coverage. Ionomer degradation was also confirmed with the XPS study.

MEA 4 was identical to MEA 1 but was cycled with catalyst AST under starving conditions for gas-flow. Significantly higher degradation rate was observed for MEA 4 due to larger ECSA loss and also larger polarization loss where the ECSA decreased by 60–63% and the cell voltage was reduced by more than 100 mV in some polarization regions at EOL. MEA 4 results indicate that gas flow-rates during catalyst ASTs are important as if flow-rates are low heterogeneous degradation of catalyst can happen.

Carbon corrosion AST was performed on MEA 2 that had HSA carbon support. The polarization curve showed a sharp voltage decrease between 100 and 500 cycles, and the cell had to be stopped early, after 1000 cycles due to lack of performance. The following were observed:

- Majority of polarization loss occurred at 100 and 500 AST cycles. This loss cannot be explained purely by Pt agglomeration and detachment (ECSA loss). This polarization loss ($\sim$160 mV at 0.2 A cm^{-2}) was mostly due to a combination of ionomer loss, carbon loss and Pt detachment.
- Significant loss of carbon was observed during the 1000 cycles, and catalyst layer thickness was reduced by half. Because of the loss of carbon the C/i interface increased from 45% at the BOL to 80% at the EOL (defined by 1000 support AST cycles).
- Pt was lost regardless whether it was in contact with ionomer or water. This is indicative of Pt agglomeration and mechanical detachment or isolation from electric or ionic domains.
- Pt/i interface dramatically decreased from 65% at 500 cycles to 20% at 1000 cycles. This is indicative of ionomer loss, as confirmed by XPS study. SO_3^- coverage monotonically decreased throughout the cycling indicating both Pt loss and also ionomer loss.

As a comparison, the same support AST was performed on a graphitized carbon support. MEA 3 performed without any seeming degradation up to 2500 cycles, but it was shut down after that due to an unexpected short circuit that ended the cell's life. In this MEA, platinum ECSA was smaller than that for MEAs 1 and 2 having high surface area carbon as larger fraction of Pt was on the surface of carbon support, indicating a smaller amount of meso and micropores within the carbon support. Differently from the previous case, here both performance and ionomer coverage were preserved through the cycling. The effect of a stable support is not only to mitigate the corrosion and the consequent ECSA loss, but also to offer a better anchoring to ionomer and preservation of ionic connection and proton availability.

Credit author contribution statement

Andrea Perego: Conceptualization, Methodology, Data curation, Writing – original draft preparation; **Arezoo Avid:** Methodology, Investigation, Writing – original draft preparation; **Divija Mamania:** Investigation; **Yechuan Chen:** Investigation; **Plamen Atanassov:** Supervision, data curation; **Hakan Yildirim:** Supervision, Writing – reviewing & editing; **Madeleine Odgaard:** Supervision, Writing – reviewing & editing; **Iryna Zenyuk:** Conceptualization; Funding acquisition; Supervision, Writing - reviewing & editing.

Declaration of Competing Interest

The authors declare that they have no known competing financial interests or personal relationships that could have appeared to influence the work reported in this paper.

Acknowledgements

Appendix A. Supporting information

Supplementary data associated with this article can be found in the online version at doi:10.1016/j.apcatb.2021.120810.

References

[1] D.-Y. Lee, A. Elgowainy, A. Kotz, R. Vijayagopal, J. Marcinkoski, Life-cycle implications of hydrogen fuel cell electric vehicle technology for medium- and heavy-duty trucks, J. Power Sources 393 (2018) 217–229, https://doi.org/10.1016/j.jpowsour.2018.05.012.

[2] X.X. Wang, M.T. Swihart, G. Wu, Achievements, challenges and perspectives on cathode catalysts in proton exchange membrane fuel cells for transportation, Nat. Catal. 2 (7) (2019) 578–589, https://doi.org/10.1038/s41929-019-0304-9.

[3] D.A. Cullen, K.C. Neyerlin, R.K. Ahluwalia, R. Mukundan, K.L. More, R.L. Borup, A. Z. Weber, D.J. Myers, A. Kusoglu, New roads and challenges for fuel cells in heavy-duty transportation, Nat. Energy 6 (5) (2021) 462–474, https://doi.org/10.1038/s41560-021-00775-z.

[4] J. Marcinkoski R. Vijayagopal J. Adams B. James J. Kopasz R. Ahluwalia. Hydrogen Class 8 Long Haul Truck Targets. 2019, 1, 31.

[5] R.L. Borup, A. Kusoglu, K.C. Neyerlin, R. Mukundan, R.K. Ahluwalia, D.A. Cullen, K.L. More, A.Z. Weber, D.J. Myers, Recent developments in catalyst-related PEM fuel cell durability, Curr. Opin. Electrochem 21 (2020) 192–200, https://doi.org/10.1016/j.coelec.2020.02.007.

[6] P. Ren, P. Pei, Y. Li, Z. Wu, D. Chen, S. Huang, Degradation mechanisms of proton exchange membrane fuel cell under typical automotive operating conditions, Prog. Energy Combust. Sci. 80 (2020), 100859, https://doi.org/10.1016/j.pecs.2020.100859.

[7] W. Schmittinger, A. Vahidi, A review of the main parameters influencing long-term performance and durability of PEM fuel cells, J. Power Sources 180 (1) (2008) 1–14, https://doi.org/10.1016/j.jpowsour.2008.01.070.

[8] G.S. Harzer, J.N. Schwämmlein, A.M. Damjanović, S. Ghosh, H.A. Gasteiger, Cathode loading impact on voltage cycling induced PEMFC degradation: a voltage loss analysis, J. Electrochem Soc. 165 (6) (2018) F3118–F3131, https://doi.org/10.1149/2.0161806jes.

[9] G. Kluger, T. Glauser, G. Krauss, R. Seeruthun, C. Perdomo, S. Arroyo, Recent advances in catalyst accelerated stress tests for polymer electrolyte membrane fuel cells, J. Electrochem Soc. 165 (7) (2018) F492–F501, https://doi.org/10.1149/2.0881807jes.

[10] L. Cheng, K. Khedekar, M. Rezaei Talarposhti, A. Perego, M. Metzger, S. Kuppan, S. Stewart, P. Atanassov, N. Tamura, N. Craig, I.V. Zenyuk, C.M. Johnston, Mapping of heterogeneous catalyst degradation in polymer electrolyte fuel cells, Adv. Energy Mater. 10 (28) (2020), 2000623, https://doi.org/10.1002/aenm.202000623.

[11] J. Huang, Z. Li, J. Zhang, Review of characterization and modeling of polymer electrolyte fuel cell catalyst layer: the blessing and curse of ionomer, Front Energy 11 (3) (2017) 334–364, https://doi.org/10.1007/s11708-017-0490-6.

[12] A. Avid, I.V. Zenyuk, Confinement effects for nano-electrocatalysts for oxygen reduction reaction, Curr. Opin. Electrochem. 25 (2021), 100634, https://doi.org/10.1016/j.coelec.2020.09.001.

[13] A. Kongkanand, M.F. Mathias, The priority and challenge of high-power performance of low-platinum proton-exchange membrane fuel cells, J. Phys. Chem. Lett. 7 (7) (2016) 1127–1137, https://doi.org/10.1021/acs.jpclett.6b00216.

[14] H. Liu, W.K. Epting, S. Litster, Gas transport resistance in polymer electrolyte thin films on oxygen reduction reaction catalysts, Langmuir 31 (36) (2015) 9853–9858, https://doi.org/10.1021/acs.langmuir.5b02487.

[15] R. Jinnouchi, K. Kudo, N. Kitano, Y. Morimoto, Molecular dynamics simulations on O2 permeation through nafion ionomer on platinum surface, Electro Acta 188 (2016) 767–776, https://doi.org/10.1016/j.electacta.2015.12.031.

[16] Y. Kurihara, T. Mabuchi, T. Tokumasu, Molecular simulation of oxygen solubility and diffusivity in Ionomer on Pt surface, ECS Trans. 69 (17) (2015) 691–699, https://doi.org/10.1149/06917.0691ecst.

[17] T. Morawietz, M. Handl, C. Oldani, P. Gazdzicki, J. Hunger, F. Wilhelm, J. Blake, K. A. Friedrich, R. Hiesgen, High-resolution analysis of ionomer loss in catalytic layers after operation, J. Electrochem Soc. 165 (6) (2018) F3139–F3147, https://doi.org/10.1149/2.0151806jes.

[18] T.Y. George, T. Asset, A. Avid, P. Atanassov, I.V. Zenyuk, Kinetic isotope effect as a tool to investigate the oxygen reduction reaction on Pt-based electrocatalysts – Part I: high-loading Pt/C and Pt extended surface, ChemPhysChem 21 (6) (2020) 469–475, https://doi.org/10.1002/cphc.201901091.

[19] S. Ott, A. Orfanidi, H. Schmies, B. Anke, H.N. Nong, J. Hübner, U. Gernert, M. Gliech, M. Lerch, P. Strasser, Ionomer distribution control in porous carbon-supported catalyst layers for high-power and low Pt-loaded proton exchange membrane fuel cells, Nat. Mater. 19 (1) (2020) 77–85, https://doi.org/10.1038/s41563-019-0487-0.

[20] A. Orfanidi, P. Madkikar, H.A. El-Sayed, G.S. Harzer, T. Kratky, H.A. Gasteiger, The key to high performance low Pt loaded electrodes, J. Electrochem Soc. 164 (4) (2017) F418–F426, https://doi.org/10.1149/2.1621704jes.

[21] A. Katzenberg, A. Chowdhury, M. Fang, A.Z. Weber, Y. Okamoto, A. Kusoglu, M. A. Modestino, Highly Permeable perfluorinated sulfonic acid ionomers for

improved electrochemical devices: insights into structure-property relationships, J. Am. Chem. Soc. 142 (8) (2020) 3742–3752, https://doi.org/10.1021/jacs.9b09170.

[22] K. Kodama, K. Motobayashi, A. Shinohara, N. Hasegawa, K. Kudo, R. Jinnouchi, M. Osawa, Y. Morimoto, Effect of the side-chain structure of perfluoro-sulfonic acid ionomers on the oxygen reduction reaction on the surface of Pt, ACS Catal. 8 (1) (2018) 694–700, https://doi.org/10.1021/acscatal.7b03571.

[23] K. Malek, T. Mashio, M. Eikerling, Microstructure of catalyst layers in PEM fuel cells redefined: a computational approach, Electrocatalysis 2 (2) (2011) 141–157, https://doi.org/10.1007/s12678-011-0047-0.

[24] C.-Y. Jung, S.-W. Choi, W.-Y. Choi, C.-W. Hong, V.R. Jothi, S.-C. Yi, Engineering ionomer homogeneously distributed onto the fuel cell electrode with superbly retrieved activity towards oxygen reduction reaction, Appl. Catal. B Environ. 298 (2021), 120609, https://doi.org/10.1016/j.apcatb.2021.120609.

[25] H. Iden, A. Ohma, An in situ technique for analyzing ionomer coverage in catalyst layers, J. Electro Chem. 693 (2013) 34–41, https://doi.org/10.1016/j.jelechem.2013.01.026.

[26] T.R. Garrick, T.E. Moylan, V. Yarlagadda, A. Kongkanand, Characterizing electrolyte and platinum interface in PEM fuel cells using CO displacement, J. Electrochem Soc. 164 (2) (2017) F60–F64, https://doi.org/10.1149/2.0551702jes.

[27] S.M. Andersen, Nano carbon supported platinum catalyst interaction behavior with perfluorosulfonic acid ionomer and their interface structures, Appl. Catal. B Environ. 181 (2016) 146–155, https://doi.org/10.1016/j.apcatb.2015.07.049.

[28] T.F. Cells, F. Cell, T. Office, F. Cells, T. Office, T.F. Cells, Fuel cell 2016 multi-year research, Dev. Demonstr. Plan 2015 (2016) 1–58.

[29] T. Jahnke, G.A. Futter, A. Baricci, C. Rabissi, A. Casalegno, Physical modeling of catalyst degradation in low temperature fuel cells: platinum oxidation, dissolution, particle growth and platinum band formation, J. Electrochem Soc. 167 (1) (2020) 013523–013528, https://doi.org/10.1149/2.0232001JES.

[30] M. Obermaier, A.S. Bandarenka, C. Lohri-Tymozhynsky, A comprehensive physical impedance model of polymer electrolyte fuel cell cathodes in oxygen-free atmosphere, Sci. Rep. 8 (1) (2018) 4933, https://doi.org/10.1038/s41598-018-23071-5.

[31] O.E. Barcia, E. D'Elia, I. Frateur, O.R. Mattos, N. Pébère, B. Tribollet, Application of the impedance model of de Levie for the characterization of porous electrodes, Electro Acta 47 (13) (2002) 2109–2116, https://doi.org/10.1016/S0013-4686(02)00081-6.

[32] P.P. Lopes, D. Strmcnik, D. Tripkovic, J.G. Connell, V. Stamenkovic, N. M. Markovic, Relationships between atomic level surface structure and stability/activity of platinum surface atoms in aqueous environments, ACS Catal. 6 (4) (2016) 2536–2544, https://doi.org/10.1021/acscatal.5b02920.

[33] T. Takeshita, Y. Kamitaka, K. Shinozaki, K. Kodama, Y. Morimoto, Evaluation of ionomer coverage on Pt catalysts in polymer electrolyte membrane fuel cells by CO stripping voltammetry and its effect on oxygen reduction reaction activity, J. Electro Chem. 871 (2020), 114250, https://doi.org/10.1016/j.jelechem.2020.114250.

[34] T. Van Cleve, G. Wang, M. Mooney, C.F. Cetinbas, N. Kariuki, J. Park, A. Farghaly, D. Myers, K.C. Neyerlin, Tailoring electrode microstructure via ink content to enable improved rated power performance for platinum cobalt/high surface area carbon based polymer electrolyte fuel cells, J. Power Sources 482 (2021), 228889, https://doi.org/10.1016/j.jpowsour.2020.228889.

[35] L. Gubler, S.M. Dockheer, W.H. Koppenol, Radical (HO•, H• and HOO•) Fformation and Ionomer degradation in polymer electrolyte fuel cells, J. Electrochem. Soc. 158 (7) (2011) B755–B758, https://doi.org/10.1149/1.3581040.

[36] H.A. Gasteiger, J.E. Panels, S.G. Yan, Dependence of PEM fuel cell performance on catalyst loading, J. Power Sources 127 (1) (2004) 162–171, https://doi.org/10.1016/j.jpowsour.2003.09.013.

[37] M. Kruk, Z. Li, M. Jaroniec, W.R. Betz, Nitrogen adsorption study of surface properties of graphitized carbon blacks, Langmuir 15 (4) (1999) 1435–1441, https://doi.org/10.1021/la980493+.

[38] N. Ramaswamy, W. Gu, J.M. Ziegelbauer, S. Kumaraguru, Carbon support microstructure impact on high current density transport resistances in PEMFC cathode, J. Electrochem Soc. 167 (6) (2020) 64515, https://doi.org/10.1149/1945-7111/ab819c.